

Monodisperse Dual Plasmonic Au@Cu_{2-x}E (E = S, Se) Core@Shell Supraparticles: Aqueous Fabrication, Multimodal Imaging, and Tumor Therapy at *in Vivo* Level

Hui Zhu,^{†,§} Yong Wang,^{‡,§} Chao Chen,^{||} Mingrou Ma,[†] Jianfeng Zeng,[‡] Shuzhou Li,^{||} Yunsheng Xia,^{*,†,||} and Mingyuan Gao^{‡,||}

[†]Key Laboratory of Functional Molecular Solids, Ministry of Education, College of Chemistry and Materials Science, Anhui Normal University, Wuhu 241000, China

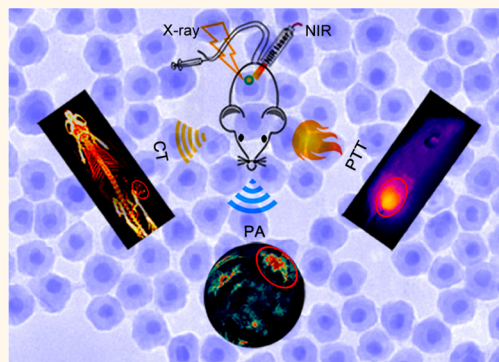
[‡]Center for Molecular Imaging and Nuclear Medicine, School for Radiological and Interdisciplinary Sciences (RAD-X), Soochow University, Collaborative Innovation Center of Radiation, Medicine of Jiangsu Higher Education Institutions, Suzhou 215123, China

^{||}School of Materials Science and Engineering, Nanyang Technological University, Singapore 639798, Singapore

Supporting Information

ABSTRACT: We herein report aqueous fabrication of well-defined Au@Cu_{2-x}E (E = S, Se) core@shell dual plasmonic supraparticles (SPs) for multimodal imaging and tumor therapy at the *in vivo* level. By means of a modified self-limiting self-assembly based strategy, monodisperse core@shell dual plasmonic SPs, including spherical Au@Cu_{2-x}S SPs, Au@Cu_{2-x}Se SPs, and rod-like Au@Cu_{2-x}S SPs, are reliably and eco-friendly fabricated in aqueous solution. Due to plasmonic coupling from the core and shell materials, the as-prepared hybrid products possess an extremely large extinction coefficient (9.32 L g⁻¹ cm⁻¹ for spherical Au@Cu_{2-x}S SPs) at 808 nm, which endows their excellent photothermal effect. Furthermore, the hybrid core@shell SPs possess the properties of good biocompatibility, low nonspecific interactions, and high photothermal stability. So, they show favorable performances for photoacoustic imaging and X-ray computed tomography imaging as well as photothermal therapy of tumors, indicating their application potentials in biological field.

KEYWORDS: dual plasmonic, supraparticles, core@shell, self-assembly, multimodal imaging, tumor therapy



Exploring fabrication strategies for core@shell hybrid nanocomposites and studying their applications are of great significance for nanoscience and nanotechnology.^{1,2} Noble metals (Au, Ag, etc.)^{3,4} and vacancy-doped copper chalcogenides (Cu_{2-x}E, $x > 0$, E = S, Se, Te)^{5,6} are two kinds of plasmonic materials and their surface plasmon resonance (SPR) arising from the collective oscillation of free electrons and free holes driven by the electromagnetic field of incident light, respectively. Recently, the hybrid entities consisting of the dual metal–semiconductor plasmonic nanoparticles (NPs) have emerged as an intriguing set of nanosuperstructures due to their synergetic properties and application potentials in biological and catalytic fields.^{7–11} To date, there are very few reports for the fabrication of well-defined metal@semiconductor core@shell dual plasmonic hybrid superstructures, and most of them are based on cation exchange reactions.^{12,13} Generally, cation exchange is a state-of-the-art method for effective fabrication of complicated nanostructures including

core@shell ones.^{14–17} However, it has three potential problems, especially for dual plasmonic metal@semiconductor hybrid structures. First of all, the products are contaminative. For obtaining Au@Cu_{2-x}E entities, Au@CdE hybrids are employed as starting templates. In the cation exchange processes, the host Cd²⁺ ions cannot be completely substituted by Cu⁺/Cu²⁺ counterparts^{12,13} due to the limit of thermodynamic equilibrium, and the impure products are unfavorable for either property study or biological applications (the residual Cd²⁺ ions are toxic). Then, the cation exchange processes are very rigorous and tedious. To avoid oxygen and water, the experimental devices should be put in a glovebox.^{12,18–20} Furthermore, harmful organometallic Cu precursors (such as

Received: May 17, 2017

Accepted: July 24, 2017

Published: July 25, 2017



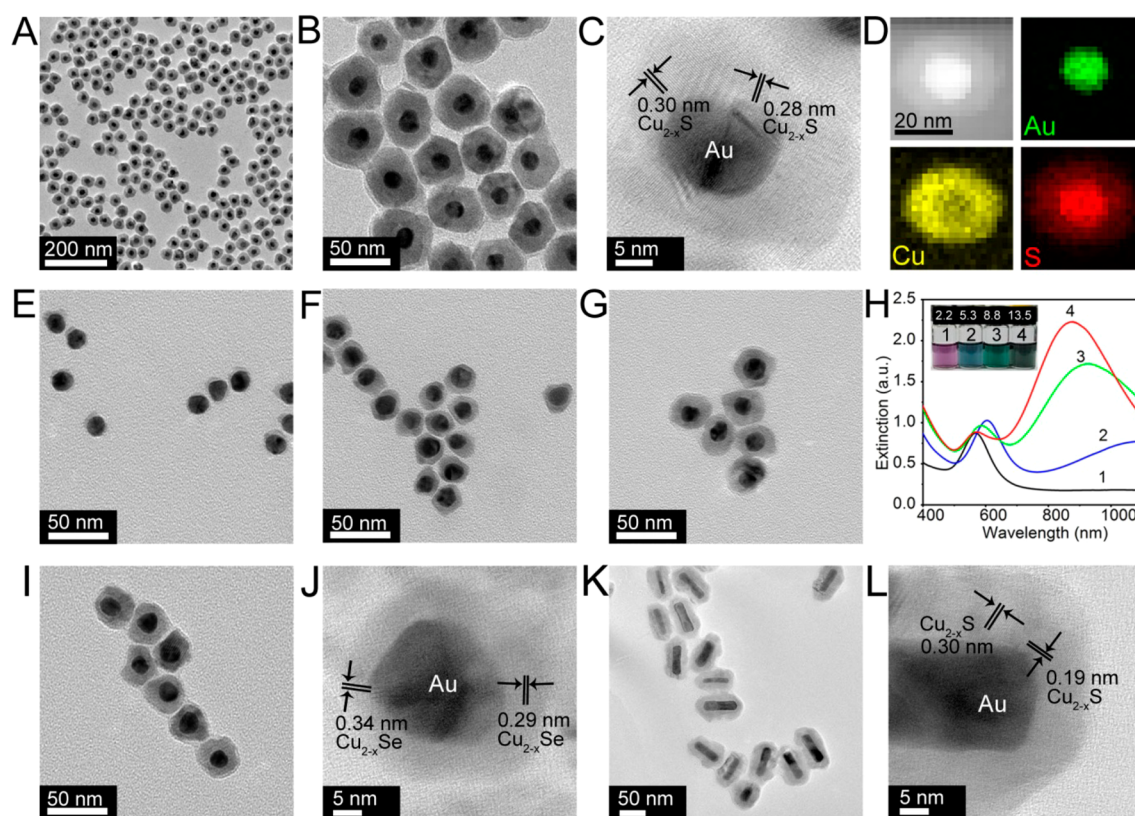


Figure 1. Characterizations of the core@shell Au@Cu_{2-x}E SPs. Large-scale (A) and small-scale (B) TEM images, HRTEM (C), and element mapping (D) of SPs-13.5. TEM images of SPs-2.2 (E), SPs-5.3 (F), and SPs-8.8 (G). (H) SPR extinction of Au@Cu_{2-x}S SPs with different shell thickness (the inset is the corresponding photo images). TEM (I) and HRTEM (J) of spherical Au@Cu_{2-x}Se SPs. TEM (K) and HRTEM (L) of rod-like Au@Cu_{2-x}S SPs.

[Cu(CH₃CN)₄]PF₆) are often employed.^{12,13,21} Last, the products are water insoluble,^{12,13} and troublesome phase transfer processes have to be conducted for biological applications. Just recently, a two-step procedure was presented for aqueous synthesis of hybrid Au–Cu_{2-x}Se NPs with different structures. Because this method is based on the reaction of Cu²⁺ cations with preformed intermediates of Au–Se “complex”, it can only be employed for the fabrication of Cu_{2-x}Se based hybrid products.²² Therefore, it is urgent to explore a fabrication system, in which well-defined dual plasmonic Au@Cu_{2-x}E core@shell superstructures can be generally and eco-friendly obtained. Such a system would greatly enrich the kit of nanofabrication and well promote the combination of dual plasmonic metal@semiconductor superstructures and biological fields.

Herein, we report a modified self-limiting self-assembly based strategy to obtain well-defined Au@Cu_{2-x}E (E = S, Se) core@shell supraparticles (SPs) in aqueous solution and further investigate their multimodal imaging and photothermal therapy (PTT) applications at both *in vitro* and *in vivo* levels. In 2011, we developed an *in situ* formation and assembly system²³ for the fabrication of various monodisperse semiconductor (CdS, CdSe, PbS, ZnSe, etc.) and hybrid noble metal@semiconductor core@shell (Au@CdS, Au@CdSe, etc.) SPs, based on the modulation effects of van der Waals attraction and electrostatic repulsion. However, this system cannot be employed for directly fabricating Au@Cu_{2-x}E core@shell nanosuperstructures. The probable reasons are too fast reaction rate and/or too high affinity between Au and Cu_{2-x}E materials, which cause the immediate and uncontrollable aggregation of the colloidal

system. To solve this problem, we herein rationally introduce an additional steric effect assisted by polymer molecules, which can effectively overcome particle aggregation and obtain well-defined Au@Cu_{2-x}E core@shell SPs. Due to the introduction of additional steric effects, it is called “a modified self-limiting self-assembly based strategy”. The proposed fabrication system is rather general, and various hybrid products including spherical Au@Cu_{2-x}S SPs, Au@Cu_{2-x}Se SPs, as well as rod-like Au@Cu_{2-x}S SPs can be reliably obtained in aqueous solution. The Au@Cu_{2-x}E SPs possess an extremely large extinction coefficient (9.32 L g^{−1} cm^{−1} for spherical Au@Cu_{2-x}S SPs) at 808 nm by plasmonic coupling of the core and shell materials, which endows their excellent photothermal effect. Due to good biocompatibility, low nonspecific interactions, and high photothermal stability, the hybrid SPs show favorable performances for photoacoustic (PA) imaging, X-ray computed tomography (CT) imaging, as well PTT for tumors, indicating their application potentials in biological and biomedical fields.

RESULTS AND DISCUSSION

The *in situ* formation and assembly system²³ can be used for fabricating various SPs including Au@CdSe core@shell ones, which has been adopted as a template for the production of dual plasmonic Au@Cu_{2-x}Se hybrids by cation exchange method, as reported by the Rodríguez-Fernández group.¹² This study implies that such a system cannot be extended to the fabrication of Au@Cu_{2-x}E core@shell superstructures. As expected, the reactive system aggregates immediately as S or Se precursors are introduced (Figure S1), which probably

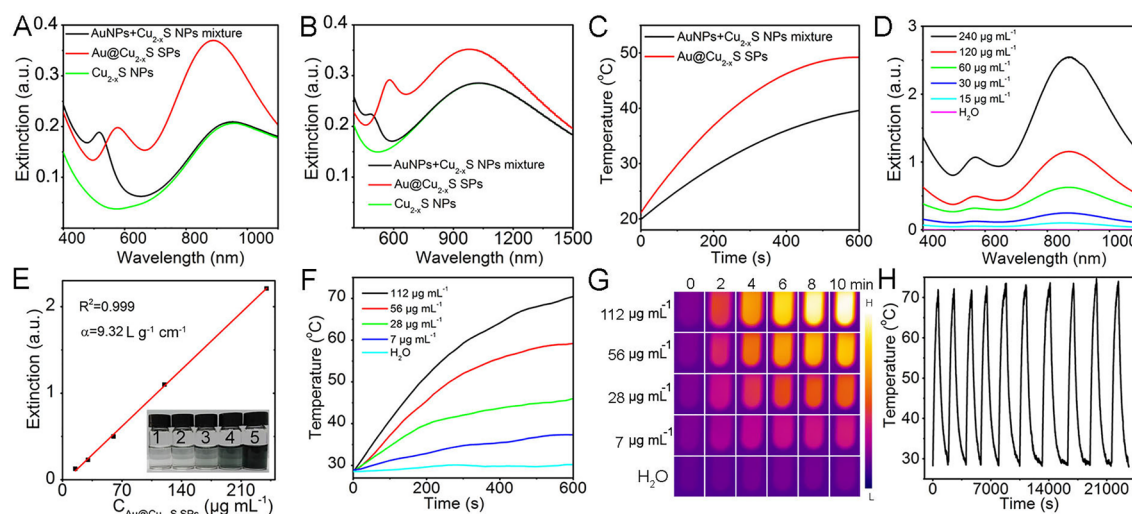


Figure 2. Optical and photothermal properties of the core@shell Au@Cu_{2-x}S SPs. Experimental (A) and FDTD calculated (B) SPR bands of the Au@Cu_{2-x}S SPs. (C) Photothermal effects of the Au@Cu_{2-x}S SPs and the physical mixture of Au and Cu_{2-x}S NPs. Concentration-dependent SPR bands (D) and extinction (E) the Au@Cu_{2-x}S SPs. Concentration-dependent photothermal effects (F, G) of the Au@Cu_{2-x}S SPs. (H) Temperature changes of the Au@Cu_{2-x}S SPs over 10 cycles of irradiation/cooling.

results from a too fast reaction rate and/or too high affinity between Au and Cu_{2-x}S materials. So, the dynamic control would be critical. Following this thought, we herein introduce an additional steric effect at the Au surface, which would decrease the particle reactivity and help to control the *in situ* self-assembly processes. The steric effect is achieved by the introduction of polyvinylpyrrolidone (PVP) or poly(styrenesulfonate) polymer molecules on the Au particle surface. Herein, Au@Cu_{2-x}S SPs fabrication was employed as an example. First, citrate capped AuNPs were first mixed with PVP molecules and incubated in 70 °C for 30 min. After PVP treatment, the SPR profile of the AuNPs keeps almost invariable (Figure S2), indicating well dispersity of the particles. Furthermore, the AuNPs' hydrodynamic size increases from 19 to 27 nm (Figure S3), and their ζ -potential value changes from -30.7 to -9.9 mV (Figure S4). These data demonstrate that PVP molecules successfully bind onto the Au surface by partially exchanging the precapped citrate groups. Then, CuSO₄·5H₂O and thioacetamide were orderly introduced to the solution containing PVP treated AuNPs (see Experimental Section). Furthermore, a synchronous reduction method was adopted for Cu⁺ doping during the formation of the semiconductor shell, which was conducted by using hydroxylamine hydrochloride as reducing agents (see Experimental Section).

As shown in the large- (Figures 1A and S5) and small-scale (Figure 1B) transmission electron microscope (TEM) images, the PVP treated AuNPs are well capped and form single-core hybrid core@shell SPs, and neither self-nucleation of shell materials nor particle aggregation is observed. Furthermore, the shell thickness can be finely tuned from 2.2 to 13.5 nm (Figure 1E–G and 1B) by adjusting the amounts of shell precursors (see Experimental Section). For simplicity, the four products are named by their shell thickness, namely SPs-2.2, SPs-5.3, SPs-8.8, and SPs-13.5, respectively. According to ICP analysis, the shell compositions of the four corresponding SPs are Cu_{1.93}S, Cu_{1.82}S, Cu_{1.54}S, and Cu_{1.22}S, respectively. Obviously, all the products are nonstoichiometric, demonstrating doping successfully by the proposed synchronous reduction method.²⁴ Figure 1C is the high resolution (HR) TEM of SPs-13.5, and

the shell exhibits distinct lattice fringes, indicating good crystallinity. In addition to contrast difference, the hybrid core@shell structure can also be well viewed by mapping of their element distribution (Figure 1D). As described in inset of Figure 1H and Figure S6, all the hybrid SPs with different shell thickness can well disperse in water solutions, and they have two distinct SPR bands at visible and NIR regions, respectively (Figure 1H). The shorter bands come from Au cores, which shift to longer wavelengths after Cu_{2-x}S coating due to the larger refractive index of the shell materials as compared with water medium. The NIR bands result from the coupling effects of the Au core and Cu_{2-x}S shell (see below). With the increase of shell thickness, the NIR bands become stronger and stronger; at the same time, they exhibit a regular hypochromatic shift due to the ratio enhancement of Cu²⁺/Cu⁺.^{12,25} It must be emphasized that the present system is different from a recent Jiang report²² in both fabrication concept and chemical principle, although similar polymer molecules are employed in the two fabrication systems. In terms of Jiang's system,²² the fabrication procedures contain two-step reactions for the formation of Cu_{2-x}Se parts. First, AuNPs react with SeO₂ and form Au–Se “complexes”. Then, the added Cu²⁺ cations react with the preformed Au–Se templates, and the Au–Cu_{2-x}Se products are obtained. Because this system is dependent on the modulation effect of Au–Se intermediates, it is limited to the fabrication of Cu_{2-x}Se based hybrid products. In contrast, for the present fabrication system, the formation of shell structures only needs a one-step reaction (see Experimental Section). More importantly, this system provides a general platform for the fabrication of dual plasmonic core@shell nanostructures, because it is based on a self-assembly strategy achieved by versatile manipulation of NPs–NPs interactions. As a result, in addition to spherical Au@Cu_{2-x}S SPs, other products, such as spherical Au@Cu_{2-x}Se SPs (Figure 1I and 1J) and rod-like Au@Cu_{2-x}S SPs (Figure 1K and 1L), can also be fabricated. Furthermore, the SPR bands of the hybrid SPs can reach a NIR-II window (1000–1400 nm) (Figure S9) due to the modulation effects of composition/morphology. These optical properties enrich the application of materials.^{26,27} The present results indicate that on the one

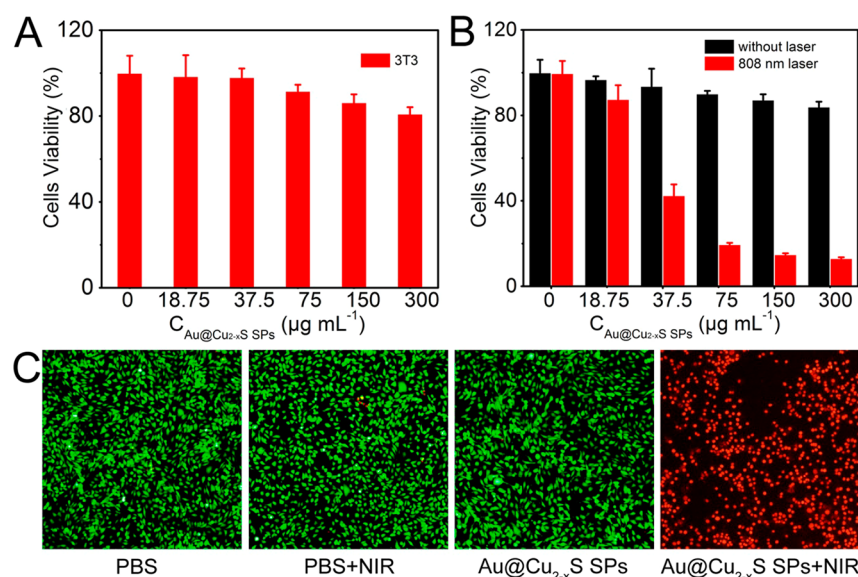


Figure 3. (A) Cell viability of normal 3T3 cells after incubation with various concentrations of the $\text{Au@Cu}_{2-x}\text{S}$ SPs ($0\text{--}300\ \mu\text{g mL}^{-1}$) for 24 h. (B) Cell viability of 4T1 cells after incubation with various concentrations of the $\text{Au@Cu}_{2-x}\text{S}$ SPs ($0\text{--}300\ \mu\text{g mL}^{-1}$) for 24 h and then irradiated with a 808 nm laser ($0.75\ \text{W cm}^{-2}$, 10 min). (C) Fluorescence microscopy images of 4T1 cells stained with live/dead kit after incubation with PBS and the $\text{Au@Cu}_{2-x}\text{S}$ SPs ($50\ \mu\text{g mL}^{-1}$) with and without 808 nm laser irradiation; live cell, green; dead cell, red.

hand, the proposed modified *in situ* formation and assembly based strategy are effective and general for the fabrication of dual plasmonic core@shell SPs, and on the other hand, the products possess well tunable composition, morphology, as well as optical property. Considering that SPs-13.5 possesses the strongest SPR band, they were employed for further study (in the following, all the used SPs are SPs-13.5). As shown in Figure 2A, the SPR intensity of the hybrid $\text{Au@Cu}_{2-x}\text{S}$ SPs is obviously higher than that of the physical mixture of Au and Cu_{2-x}S NPs. To better understand this property, finite-difference time-domain calculations (FDTD) were then performed to study the interactions of the two kinds of plasmonic materials. As shown in Figure 2B, the FDTD calculation results are consistent with that of experiment data on the whole, which indicates the coupling effects of Au and Cu_{2-x}S materials.^{9,13} So, the hybrid SPs exhibit an enhanced photothermal effect as compared with the physical mixture of Au and Cu_{2-x}S NPs (Figure 2C). As described in Figure 2D and 2E, the SPs' SPR intensity at 808 nm is linearly increased with the enhancement of their concentration, indicating excellent dispersity of the SPs.

The extremely large extinction coefficient at NIR region suggests that the hybrid SPs have a pronounced photothermal conversion capability. As shown in Figure 2F and 2G, the SPs exhibit a concentration-dependent photothermal conversion behavior. It should be noted that the water solution shows an obvious temperature rise (even the dosage of the used $\text{Au@Cu}_{2-x}\text{S}$ SPs is as low as $7\ \mu\text{g mL}^{-1}$), and the solution can be heated to more than $70\ ^\circ\text{C}$ within 10 min in the presence of $112\ \mu\text{g mL}^{-1}$ $\text{Au@Cu}_{2-x}\text{S}$ SPs. Based on Figure S12, the photothermal conversion efficiency is 52.1%, which is at least comparable and even better than that of previously reported $\text{Au@Cu}_{2-x}\text{S}$ core@shell particles synthesized by the cation exchange method.¹³

Photothermal stability is of great importance for photothermal agents during PA imaging and/or PTT treatment. To assess the photothermal stability of the hybrid core@shell SPs, the temperature profiles of their solution were recorded for 10

successive cycles of heating/cooling processes. As shown in Figure 2H, the $\text{Au@Cu}_{2-x}\text{S}$ core@shell SPs exhibit highly stable photothermal conversion capability during 10 cycles of testing. Furthermore, their morphology, SPR profile, and hydrodynamic size keep rather well after 10 cycles of photothermal conversion (Figure S13). In contrast, Au nanorods, one of often used PTT agents, tend to deform and melt during laser exposure.²⁸ Herein, the particularly stable photothermal performances of the SPs can be attributed to three reasons. First, the SPs have a spherical and five-fold twin crystalline Au core. Second, the SPs possess a well-defined core@shell structure. Third, a CuS instead of Cu_2S dominant shell is also critical, because the former is more stable at ambient conditions.

For biological applications, the dispersion stability and nonspecific issues should be well concerned.^{29–31} As shown in Figure S14, the $\text{Au@Cu}_{2-x}\text{S}$ SPs can well disperse in different mediums (aqueous solution, phosphate buffered saline (PBS) solution, pure Dulbecco's Modified Eagle's Medium (DMEM), and fetal bovine serum (FBS) solution) and keep stable even for 5 days of incubation. Furthermore, the SPs show no obvious hydrodynamic size increase in various mediums including DMEM and FBS (Figure S14A), indicating low nonspecific interactions of the as-prepared SPs. Herein, the favorable dispersion stability and low nonspecific interactions are mainly ascribed to their PVP capped surface (Figure S15): On the one hand, the steric effect from bulky PVP molecules can effectively prevent the SPs from aggregating each other, and on the other hand, the PVP capped SPs' surface possesses very low surface charge (the ξ -potential value is only 0.3 mV, Figure S16), which is adverse to electrostatic adsorption of various biomolecules. Furthermore, the as-prepared hybrid SPs are highly biocompatible. As shown in Figure 3A, the cell viability of normal 3T3 cells is only reduced about 20% even after exposure to a $300\ \mu\text{g mL}^{-1}$ solution of the $\text{Au@Cu}_{2-x}\text{S}$ SPs for 24 h. However, about 90% of murine breast cancer 4T1 cells were killed significantly by the increased concentration of the $\text{Au@Cu}_{2-x}\text{S}$ SPs after laser irradiation (808 nm, $0.75\ \text{W cm}^{-2}$)

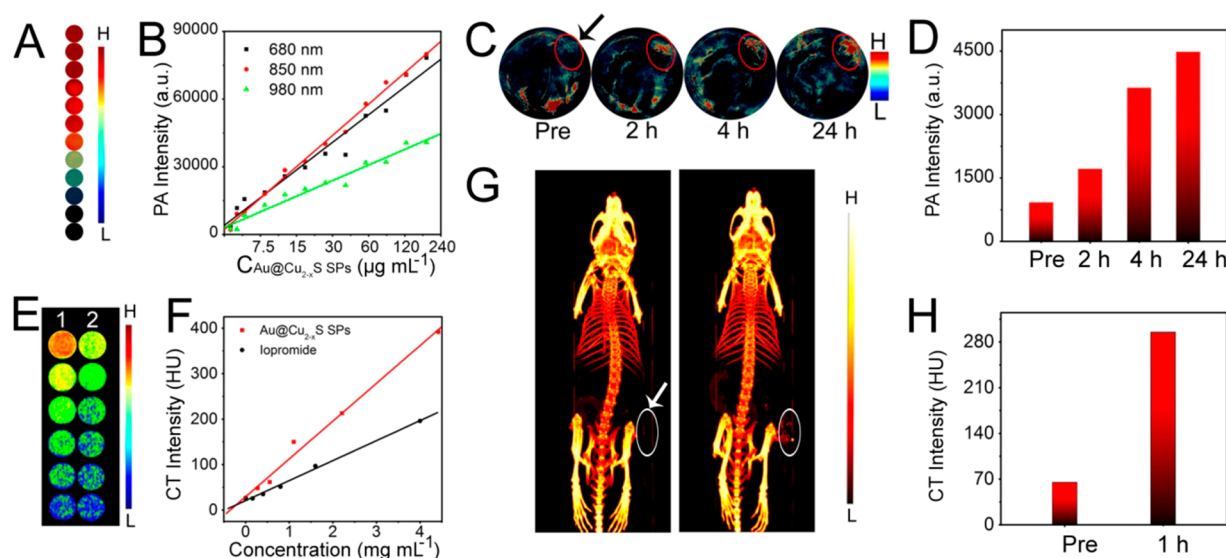


Figure 4. *In vitro* and *in vivo* multimodal imaging performances of the Au@Cu_{2-x}S SPs. (A) *In vitro* PA images of the SPs in different concentrations using 850 nm excitation wavelength, which corresponds to the red spots shown in (B). (B) Concentration-dependent *in vitro* PA signals of the SPs using different excitation wavelengths. (C) *In vivo* PA images of tumor (highlighted by red circles) from a 4T1 tumor-bearing mouse collected before and after tail vein injection of the SPs solution at different time points. (D) The intensities of PA signals corresponding to (C). (E) *In vitro* CT images of the SPs (1) and iopromide (2) in different concentrations, which corresponds to the red spots shown in (F). (F) Concentration-dependent *in vitro* CT signals of iopromide and the SPs. (G) 3D *in vivo* CT mouse images of a tumor (indicated by the white circles) before (left) and after (right) intratumoral injection of the SPs. (H) The intensities of CT signals corresponding to (G).

for 10 min (red bars, Figure 3B). Furthermore, no obvious cytotoxicity was observed in the control group without NIR irradiation (black bars, Figure 3B). The PTT effect of the SPs can be intuitively presented by live/dead cell staining. As shown in Figure 3C, almost no cell killing is found in PBS, laser only, and the SPs only groups (green fluorescence). On the contrary, for the Au@Cu_{2-x}S SPs + NIR laser group, almost all the cells are destroyed and display a red fluorescence. These findings at *in vitro* level indicate that the hybrid SPs have great potential application as one of effective PTT agents for *in vivo* tumor therapy.

Apart from PTT, the distinct SPR band at NIR region also makes the hybrid Au@Cu_{2-x}S SPs useful for PA imaging. PA imaging is an imaging technique which is based on the thermoelastic expansion of tissues directed by NIR light responsive phototherapy agents. Compared with fluorescence, the PA signal possesses a higher tissue penetration depth (~7 cm).³² To evaluate the PA imaging performances, the PA signals from the solutions containing different concentrations of the SPs were first acquired upon excitation at 680, 850, and 980 nm (Figure 4B), respectively, and one of the corresponding images is shown in Figure 4A (850 nm excitation). The excellent linearity between PA intensity and the SPs' concentrations is in favor of quantitative imaging. Then, for *in vivo* PA imaging, the Au@Cu_{2-x}S SPs (200 μ L, 2.0 mg mL⁻¹) were intravenously injected into the mice bearing 4T1 tumors. Then, the PA imaging signals were collected at different times (pre-injection, and 2, 4, and 24 h post-injection). As shown in Figure 4C and 4D, the PA signal intensities in the tumor area were enhanced gradually within the inspection time, suggesting that the Au@Cu_{2-x}S SPs can be located in the tumor by an efficient penetration and retention effect.

In addition, Au element possesses a larger X-ray attenuation coefficient (5.16 cm²·kg⁻¹ at 100 keV) than that of clinically used iopromide contrast agent (I: 1.94 cm²·kg⁻¹ at 100

keV),³³ which endows the hybrid SPs with favorable CT imaging performances (Figure 4E). As described in Figure 4F, the Hounsfield unit (HU) values also increase linearly with the concentrations of the SPs. The slope is as large as 91.9 HU L g⁻¹, which is more than 2 times larger than that of iopromide (42.27 HU L g⁻¹). Regarding the CT enhancement contrast of the SPs *in vivo*, an intratumoral injection of 50 μ L 9.2 mg mL⁻¹ Au@Cu_{2-x}S SPs well increased the tumor signal (Figure 4G). Based on the quantitative depiction shown in Figure 4H, the HU values are increased from 65 to 295 post-injection.

The above multimodal imaging performances of the Au@Cu_{2-x}S SPs are significant not only for tumor diagnosis but also for the corresponding therapy by photothermal effect. Due to the specific localization in the tumor of the Au@Cu_{2-x}S SPs, the PTT efficiency of the Au@Cu_{2-x}S SPs was then evaluated *in vivo*. In detail, either the Au@Cu_{2-x}S SPs (200 μ L, 2.0 mg mL⁻¹) or PBS were intravenously injected into mice bearing 4T1 tumors, which were divided into four groups ($n = 5$), namely, mice injected with PBS (group 1, PBS), mice treated with NIR laser irradiation after PBS injection (group 2, PBS + NIR), mice injected with the SPs (group 3, SPs), and mice treated with NIR laser irradiation after the SPs injection (group 4, SPs + NIR). Herein, all time intervals from the SPs/PBS injection to the therapeutic laser irradiations were 24 h, and all the irradiations lasted for 5 min (808 nm, 1.5 W cm⁻²).

During the NIR laser irradiation, the full-body thermal images were monitored by an infrared thermal camera. As shown in Figure 5A (above), the temperature of tumor site is dramatically enhanced for group 4; in contrast, the control group of the PBS injection (bottom of Figure 5A) does not exhibit an obvious temperature increase after the same laser irradiation. Furthermore, the temperature of the tumor site can be enhanced to about 60 °C with only 5 min irradiation (Figure 5B), which is high enough for killing tumor cells. To better understand the PTT performances, the tumor growth curves of

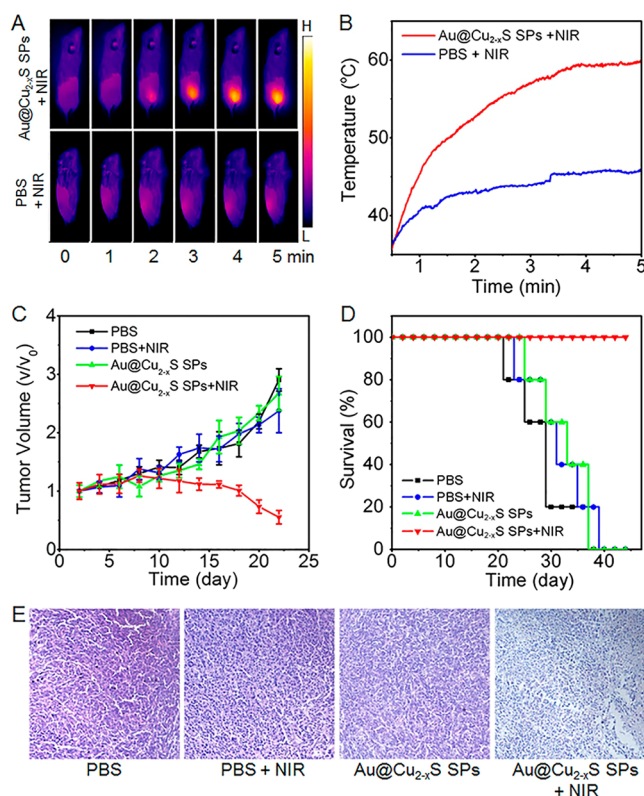


Figure 5. *In vivo* photothermal therapy of tumors with Au@Cu_{2-x}S SPs. (A) Infrared thermal images and (B) temperature curves of 4T1 tumor after the mice intravenously injected with the hybrid SPs solution (200 μ L, 2.0 mg mL⁻¹) and then laser irradiated (808 nm, 1.5 W cm⁻²) for 5 min. PBS injection is employed as control. (C) Tumor growth inhibition profiles of 4 groups of mice ($n = 5$) with time post-treatments. Relative tumor volume was normalized to their initial sizes. (D) Survival rates of 4 groups of mice ($n = 5$) with post-treatment time. (E) H&E staining of tumor sections from different groups of mice sacrificed at 12 h of treatment.

each group are studied and shown in Figure 5C. In terms of group 4, the tumor volume can be well controlled in the first 10 days, which was then decreased about 50% 22 days post-treatment. In contrast, for groups 1–3, the tumor volumes increase about 2–3 times in the same time. The substantial therapeutic effect can also be visually observed by mice appearance, as shown in Figure S17. These data clearly demonstrate that the Au@Cu_{2-x}S SPs have great potential in PTT applications.

During the period of treatment, we continually monitored the survival rates of the mice from the different groups, which could help us to better assess the therapy performances of the SP-directed tumor eradication. As shown in Figure 5D, the mice of groups 1–3 are dead around 40 days post-treatment, which probably results from the malignant proliferation and/or abnormal lung metastasis of the tumor; in contrast, the lifetime of the mice from group 4 can be substantially prolonged to 60 days post-treatment. The results further demonstrated the positive effects of the SPs for tumor therapy.

To better demonstrate the *in vivo* PTT efficiency of the SPs on tumor therapy by laser irradiation, the histopathology changes of tumor tissues after 1 day treatment were examined by hematoxylin and eosin (H&E) staining. As shown in Figure 5E, for the mice from group 4, it is observed that the tumor is damaged seriously, and the intercellular spaces are widened

irregularly, which is well in agreement with the observation of inhibiting the tumor growth in the earlier stage of PTT.

It is accepted that *in vivo* toxicity effects are always one of the major concerns for *in vivo* imaging and/or therapy applications.³⁴ So, we then studied the long-term biodistribution of the SPs *in vivo* by ICP-MS technique. Herein, we employed healthy BALB/c mice as a model system. The Au@Cu_{2-x}S SPs (200 μ L, 2.0 mg mL⁻¹) were injected into each mouse *via* the tail vein, and the biodistributions of Cu element were then quantified by ICP-MS. As shown in Figure S19, the SPs accumulation in several organs including liver, spleen, and kidney is dramatic. The results probably demonstrate that the Au@Cu_{2-x}S SPs mainly accumulate in the organs containing macrophages with high endocytosis activity (e.g., liver and kidney) and further clear away the SPs from these organs. Sequentially, the amounts of the accumulated Au@Cu_{2-x}S SPs in these organs/tissues significantly decreased in about 7 days, and the SPs could be almost completely cleared 60 days post-administration. The long-term biodistribution results suggest that the Au@Cu_{2-x}S SPs are promising for *in vivo* experiments.

Finally, to evaluate whether the SPs were potentially toxic, complete necropsies and hematology were conducted based on humanely euthanized control and treated mice. The exposure dose in mice was about 16 μ g SPs/g mouse weight. The major organs including heart, liver, spleen, lung, and kidney were well examined at 1, 7, and 60 days post-injection of the Au@Cu_{2-x}S SPs (200 μ L, 2.0 mg mL⁻¹). The histopathology shown in Figure S20 reveals no obvious organ abnormalities and/or lesions for the Au@Cu_{2-x}S SPs treated mice as compared with the control group. Furthermore, abnormalities of red/white blood cells or serum chemistry are also not detected (Figure S21), which is often relevant with organ damage and/or inflammation. In addition, the concentration level of creatinine (one of indicators for kidney injury) was drastically increased at day 1, but then decreased to normal levels after 7 days, which probably indicated an acute response of the kidney to the SPs. According to the above systematic animal toxicity evaluation, the hybrid Au@Cu_{2-x}S SPs are highly biocompatible even at the *in vivo* level, which is probably competent as one of the multimodal imaging and PTT agents for clinical applications.

CONCLUSIONS

In summary, by rationally introducing steric effects on AuNPs surface, a modified *in situ* self-assembly system is presented for the fabrication of well-defined and monodisperse core@shell dual plasmonic Au@Cu_{2-x}S SPs in aqueous solution. Due to the extremely large extinction coefficient in the NIR region, high photothermal conversion efficiency, favorable biocompatibility, low nonspecific interactions, as well as high photothermal stability, the as-prepared hybrid SPs show favorable application potentials in multimodal imaging and PTT performances at both *in vitro* and *in vivo* levels. This contribution demonstrates that aqueous solution based self-assembly is a powerful fabrication strategy for complicated nanosuperstructures, especially for biological applications.

EXPERIMENTAL SECTION

Materials. CuSO₄·5H₂O, HAuCl₄·3H₂O, NaOH, sodium citrate, hydroxylamine hydrochloride, thioacetamide, polyvinylpyrrolidone (PVP, MW 40,000), *N,N*-dimethylselenourea, and poly(styrenesulfonate) (PSS, MW 70,000) were purchased from Alfa Aesar. Hexadecyl trimethylammonium Bromide (CTAB), ascorbic acid, NaBH₄, AgNO₃, and HCl were acquired from Shanghai Reagent

Company. All chemicals were used as received. All solutions were prepared in Milli-Q water (Millipore, USA, resistivity >18 MΩ·cm).

Characterization Methods and Instruments. SPR spectra were recorded with a PerkinElmer Lambda 750 UV–vis–NIR spectrophotometer. Transmission electron microscope (TEM) and high resolution (HR) TEM images were captured by an FEI Tecnai F20 transmission electron microscope operating at an acceleration voltage of 200 kV. X-ray powder diffraction (XRD) patterns were characterized with a Shimadzu XRD-6000 X-ray diffractometer equipped with Cu Kα1 radiation ($\lambda = 0.15406$ nm). The hydrodynamic size and ξ -potential values were measured at 25 °C with a Malvern Zetasizer Nano ZS90 equipped with a solid state He–Ne laser ($\lambda = 633$ nm). Fourier transform infrared (FTIR) spectra (4000–400 cm^{−1}) were recorded by a Magna-560 spectrometer (Nicolet, Madison, WI, USA). The concentration of Au@Cu_{2−x}S SPs was determined by inductively coupled plasma-mass spectroscopy (ICP-MS) (Thermo Elemental, UK). Photoacoustic imaging (PA) and X-ray computed tomography imaging (CT) mapping were performed using a MSOT INVISO-256 (iThera Medical) and a CT (MILABS), respectively.

The Fabrication of Spherical Au Cores. Spherical AuNPs were synthesized based on a previous report.³⁵ Briefly, HAuCl₄ (2.5×10^{-5} mol) was dissolved in 99 mL water in a 250 mL flask. The solution was boiled under stirring, and the amount of 8.75×10^{-5} mol sodium citrate (dissolved in 1 mL water) was added quickly. The solution was boiled for an additional 30 min. After cooling to room temperature, 0.2 g PVP (or PSS) dissolved in 10 mL water was added and incubated in 70 °C for 30 min under stirring.

Synthesis, Purification, and Modification of AuNRs. AuNRs were synthesized using a modified seed growth method.^{36,37} Specifically, the seed solution was first obtained by the addition of HAuCl₄ solution (0.01 M, 0.25 mL) into CTAB solution (0.1 M, 9.75 mL) in a 50 mL erlenmeyer flask. A freshly prepared, ice-cold NaBH₄ solution (0.01 M, 0.6 mL) was then introduced quickly into the mixture solution, followed by rapid inversion for 2 min. The resultant seed solution was kept in a 30 °C water bath for 2 h before use. To grow AuNRs, HAuCl₄ (0.01 M, 7.5 mL) and AgNO₃ (0.01 M, 1.2 mL) were first mixed with CTAB (0.1 M, 150 mL) in a 250 mL plastic tube. Then, HCl (1.0 M, 3 mL) was added for pH adjustment of the growth solution, followed by the addition of ascorbic acid (0.1 M, 1.2 mL). After the growth solution was mixed by inversion, the Au seed solution (0.21 mL) was rapidly injected. The resultant solution was gently mixed for 10 s and left undisturbed 12 h in 30 °C water bath.

For purification and modification of the AuNRs, 5 mL of the AuNRs solution was collected by centrifugation at 8000 rpm for 10 min, and it was further washed two times by water. The obtained precipitate was redispersed into 0.15 wt % PSS solution, and its concentration was estimated by Lambert–Beer law.

Synthesis of Au@Cu_{2−x}S SPs. The fabrication of Au@Cu_{2−x}S SPs has been employed as an example. First, 2.0×10^{-5} mol of sodium citrate and 9.0×10^{-6} mol of CuSO₄·5H₂O were added into a 40 mL solution containing the PVP treated AuNPs, followed by adjusting the pH to 9.3 with 0.5 mol L^{−1} NaOH. After the mixture solution was deaerated by bubbling nitrogen for 15 min, 3.0×10^{-6} mol of thioacetamide and 3.0×10^{-5} mol hydroxylamine hydrochloride were injected under continuous stirring. The resulting solution was further heated to 70 °C and refluxed under flowing nitrogen for 12 h. These processes were repeated several times to obtain shell layers with different thicknesses. The rod-like Au@Cu_{2−x}S SPs could also be obtained by replacement of the spherical Au cores by the above modified AuNRs. For spherical Au@Cu_{2−x}Se SPs fabrication, the procedures were similar to those of Au@Cu_{2−x}S SPs except for two points. First, PSS treated Au particles were employed as seeds, and then, N,N-dimethylselenourea was used as Se precursors.

In Vitro Cytotoxicity Assay of the Au@Cu_{2−x}S SPs. MTT assays were conducted to evaluate the cytotoxicity of the Au@Cu_{2−x}S SPs. In detail, 4T1 cells were first seeded in 96-well plates with a density of $\sim 8 \times 10^3$ cells per well and cultured for 24 h in DMEM supplemented with 10% FBS. Then, the cells were washed with PBS and incubated with the Au@Cu_{2−x}S SPs at different concentrations at 37 °C for 24 h.

Subsequently, the cells were washed twice with PBS and cultured in DMEM supplemented by 10% FBS for 48 h. Then, 100 μ L MTT with a concentration of 0.5 μ g mL^{−1} was added and allowed to react with the cells for 4 h before the addition of 100 μ L DMSO to dissolve the precipitates. The absorption of each solution was measured at 490 nm on a microplate reader (Thermo, Varioskan Flash).

In Vitro Photothermal Ablation of Cancer Cells. 4T1 cells were incubated with five different concentration Au@Cu_{2−x}S SPs solutions (18.75, 37.5, 75, 150, and 300 μ g mL^{−1}) for 24 h, and then the cells were washed with PBS, followed by a 10 min irradiation (808 nm, 0.75 W cm^{−2}). After another 24 h incubation, the cell viability was evaluated using the standard MTT assay. A live/dead staining kit was employed to differentiate the living cells and dead cells on a fluorescence microscope (Leica).

Photothermal Effect, Photostability, and Photothermal Conversion Efficiency. To evaluate the photothermal effects of the Au@Cu_{2−x}S SPs, the SPs solutions with concentrations of 0, 7, 28, 56, and 112 μ g mL^{−1} were irradiated under an 808 nm laser (0.75 W cm^{−2}, 10 min), and the temperature was measured via an infrared thermal imaging instrument (FLIR, A65), respectively. To evaluate the photostability, a solution containing the SPs (120 μ g mL^{−1}) in a flow tube was irradiated by an 808 nm laser (0.75 W cm^{−2}) for 10 min (LASER ON) and then natural cooling to room temperature without irradiation (LASER OFF). Subsequently, the additional nine LASER ON/OFF cycles were further repeated to test the photostability.

To evaluate the photothermal conversion efficiency, the temperature change of 1.0 mL aqueous dispersion (41 μ g mL^{−1}) was recorded as a function of time under continuous irradiation by the 808 nm laser with a power density of 0.75 W cm^{−2} until the solution reached a steady-state temperature, and the laser was turned to cool down to room temperature. The temperature was monitored via an infrared thermal imaging instrument. The photothermal conversion efficiency, η , was calculated using eqs 1–4:³⁸

$$\eta = \frac{hS(T_{\max, \text{NPs}} - T_{\max, \text{solvent}})}{I(1 - 10^{-A_{808}})} \quad (1)$$

$$\tau_s = \frac{m_D C_D}{hS} \quad (2)$$

$$t = -\tau_s \ln \theta \quad (3)$$

$$\theta = \frac{T - T_{\text{surr}}}{T_{\max, \text{NPs}} - T_{\text{surr}}} \quad (4)$$

where h is the heat transfer coefficient, S is the surface area of the container, $T_{\max, \text{NPs}}$ and $T_{\max, \text{solvent}}$ are maximum steady-state temperature for NPs solution and water, which are 42.87 and 25.09 °C, respectively. I is the incident laser power (0.75 W cm^{−2}), and A_{808} is the absorbance of the SPs at 808 nm ($A_{808} = 0.37$). τ_s is the sample system time constant, and m_D and C_D are the mass (1.0 g) and heat capacity (4.2 J g^{−1}) of the deionized water used as the solvent, respectively. θ is the dimensionless driving force temperature, T_{surr} is the ambient temperature of the surroundings, T is a temperature for NPs solutions at a constant cooling time (t), and τ_s can be determined by applying the linear time data from the cooling period vs $-\ln \theta$ ($\tau_s = 333.2$ s). Evaluating of photothermal conversion efficiency with cooling data can avoid the thermal dissipation effect during heating. The photothermal conversion efficiency of Au@Cu_{2−x}S SPs was calculated according to eq 5:

$$\eta = \frac{m \cdot c \cdot (T_{\max} - T_{\max, \text{H}_2\text{O}})}{I \cdot (1 - 10^{-A_{808}}) \cdot \tau_s} = \frac{1 \times 4.2 \times (42.87 - 25.09)}{0.75 \times (1 - 10^{-0.37}) \times 333.2} \times 100\% = 52.1\% \quad (5)$$

Animal Model. Eight week-old female BALB/c mice were anaesthetized and subcutaneous injected in the right buttock with 50 μ L 4T1 cells suspension ($\sim 5 \times 10^6$ cells). Ten days later, the tumor imaging studies were carried out.

In Vivo Photoacoustic Imaging. For *in vivo* PA imaging, 4T1 tumor-bearing mice with hair removed were anesthetized by 1.5% isoflurane and then were injected with the Au@Cu_{2-x}S SPs (2.0 mg mL⁻¹, 0.2 mL) *via* the tail vein. The administered mice were imaged using the MSOT INVISIO-256 system (iThera Medical) at different time points. Ten slices were obtained at each position and averaged to minimize the influence of animal movement in the images.

CT Imaging. *In vitro*, the CT contrast efficacy of Au@Cu_{2-x}S SPs was compared with clinical iopromide using the same element concentrations of 0.277, 0.553, 1.105, 2.21, and 4.42 mg mL⁻¹. For *in vivo* CT imaging, 4T1 tumor-bearing mice were anesthetized by 1.5% isoflurane and placed in an animal bed. Au@Cu_{2-x}S SPs (50 μ L, 9.2 mg mL⁻¹) were then intratumorally injected for CT imaging. The images were scanned in an accurate mode using a full angle, three frames averaging, a 615 mA tube current, and a 55 kV tube voltage.

Biosafety Assessment. Healthy female BALB/c mice ($n = 5$) were purchased, maintained, and handled by the protocols approved by the Institutional Animal Care/User Ethical Committee of Soochow University. Mice were intravenously injected with 200 μ L, 2.0 mg mL⁻¹ Au@Cu_{2-x}S SPs solution or saline (200 μ L, control group) and were divided into two groups ($n = 5$). Blood was collected (days 1, 7, 60) from the mice, followed by centrifugation at 3000 rpm for 10 min. The supernatant plasma fraction was stored at -80 °C for biochemistry analysis (alanine aminotransferase (ALT), aspartate aminotransferase (AST), albumin, globulin, total protein, and urea). In addition, whole blood (60 μ L) was collected, diluted, and analyzed using a hematology analyzer (Sysmex XN-3000, IL, USA). Hematology parameters including white blood cell count, red blood cell count, hematocrit, and platelets were measured. To investigate histopathology, mice were anesthetized and sacrificed, and the major organs (heart, liver, spleen, lungs, and kidneys) were harvested. They were weighed and fixed in 4% formaldehyde solution, embedded in paraffin, and sectioned into slices, which were stained by H&E staining for pathological analysis.

Stability of the Au@Cu_{2-x}S SPs *In Vivo*. First, the Au@Cu_{2-x}S SPs (2 mL, 300 μ g mL⁻¹) were injected into the mice *via* the tail vein. Second, its urine and feces were carefully collected within 24 h. Third, to fully break up the feces, a 30 min ultrasonic process was conducted. Then, the obtained products were centrifuged by a low speed (800 rpm, 10 min) for the remove of bulky impurities. The same centrifugation processes were performed for urine. Fourth, both the treated feces and urine were dialyzed for 48 h, respectively. Finally, the purified urine and feces were characterized by TEM technique.

ASSOCIATED CONTENT

Supporting Information

The Supporting Information is available free of charge on the ACS Publications website at DOI: 10.1021/acsnano.7b03369.

Theoretical calculation details and supplementary figures and tables (PDF)

AUTHOR INFORMATION

Corresponding Author

*E-mail: xiayuns@mail.ahnu.edu.cn.

ORCID

Shuzhou Li: 0000-0002-2159-2602

Yunsheng Xia: 0000-0002-7877-9718

Mingyuan Gao: 0000-0002-7360-3684

Author Contributions

[§]H.Z. and Y.W. are cofirst authors and contributed equally.

Notes

The authors declare no competing financial interest.

ACKNOWLEDGMENTS

Y.X. acknowledges support from the National Natural Science Foundation of China (no. 21422501) and Foundation for Innovation Team of Bioanalytical Chemistry. Y.W. gratefully acknowledges National Natural Science Foundation of China (21505096), National Key Research Program of China (2016YFC0101200), Postdoctoral Science Foundation of China (2015M571796 and 2015T80575). M.G. acknowledges support from the National Natural Science Foundation of China (81530057). S.L. and C.C. gratefully acknowledge support from MOE Tier1 (RG107/15 and RG2/16).

REFERENCES

- (1) Chaudhuri, R. G.; Paria, S. Core/Shell Nanoparticles: Classes, Properties, Synthesis Mechanisms, Characterization, and Applications. *Chem. Rev.* **2012**, *112*, 2373–2433.
- (2) Liu, Y.; Tang, Z. Multifunctional Nanoparticle@ MOF Core–Shell Nanostructures. *Adv. Mater.* **2013**, *25*, 5819–5825.
- (3) Daniel, M. C.; Astruc, D. Gold Nanoparticles: Assembly, Supramolecular Chemistry, Quantum-Size-Related Properties, and Applications toward Biology, Catalysis, and Nanotechnology. *Chem. Rev.* **2004**, *104*, 293–346.
- (4) Eustis, S.; El-Sayed, M. A. Why Gold Nanoparticles are More Precious than Pretty Gold: Noble Metal Surface Plasmon Resonance and Its Enhancement of the Radiative and Nonradiative Properties of Nanocrystals of Different Shapes. *Chem. Soc. Rev.* **2006**, *35*, 209–217.
- (5) Luther, J. M.; Jain, P. K.; Ewers, T.; Alivisatos, A. P. Localized Surface Plasmon Resonances Arising from Free Carriers in Doped Quantum Dots. *Nat. Mater.* **2011**, *10*, 361–366.
- (6) Hsu, S.; On, K.; Tao, A. R. Localized Surface Plasmon Resonances of Anisotropic Semiconductor Nanocrystals. *J. Am. Chem. Soc.* **2011**, *133*, 19072–19075.
- (7) Liu, X.; Lee, C.; Law, W. C.; Zhu, D.; Liu, M.; Jeon, M.; Kim, J.; Prasad, P. N.; Kim, C.; Swihart, M. T. Au–Cu_{2-x}Se Heterodimer Nanoparticles with Broad Localized Surface Plasmon Resonance as Contrast Agents for Deep Tissue Imaging. *Nano Lett.* **2013**, *13*, 4333–4339.
- (8) Cui, J.; Li, Y.; Liu, L.; Chen, L.; Xu, J.; Ma, J.; Fang, G.; Zhu, E.; Wu, H.; Zhao, L.; Wang, L.; Huang, Y. Near-Infrared Plasmonic-Enhanced Solar Energy Harvest for Highly Efficient Photocatalytic Reactions. *Nano Lett.* **2015**, *15*, 6295–6301.
- (9) Ding, X.; Liow, C. H.; Zhang, M.; Huang, R.; Li, C.; Shen, H.; Liu, M.; Zou, Y.; Gao, N.; Zhang, Z.; Li, Y.; Wang, Q.; Li, S.; Jiang, J. Surface Plasmon Resonance Enhanced Light Absorption and Photothermal Therapy in the Second Near-Infrared Window. *J. Am. Chem. Soc.* **2014**, *136*, 15684–15693.
- (10) Motl, N. E.; Bondi, J. F.; Schaak, R. E. Synthesis of Colloidal Au–Cu₂S Heterodimers *via* Chemically Triggered Phase Segregation of AuCu Nanoparticles. *Chem. Mater.* **2012**, *24*, 1552–1554.
- (11) Kim, Y.; Park, K. Y.; Jang, D. M.; Song, Y.; Kim, H. S.; Cho, Y. J.; Myung, Y.; Park, J. Synthesis of Au–Cu₂S Core–Shell Nanocrystals and Their Photocatalytic and Electrocatalytic Activity. *J. Phys. Chem. C* **2010**, *114*, 22141–22146.
- (12) Muhammed, M. A. H.; Döblinger, M.; Rodríguez-Fernández, J. Switching Plasmons: Gold Nanorod–Copper Chalcogenide Core–Shell Nanoparticle Clusters with Selectable Metal/Semiconductor NIR Plasmon Resonances. *J. Am. Chem. Soc.* **2015**, *137*, 11666–11677.
- (13) Ji, M.; Xu, M.; Zhang, W.; Yang, Z.; Huang, L.; Liu, J.; Zhang, Y.; Gu, L.; Yu, Y.; Hao, W.; Zheng, P.; Zhu, L.; Zhang, H. J. Structurally Well-Defined Au@Cu_{2-x}S Core–Shell Nanocrystals for Improved Cancer Treatment Based on Enhanced Photothermal Efficiency. *Adv. Mater.* **2016**, *28*, 3094–3101.
- (14) Son, D. H.; Hughes, S. M.; Yin, Y.; Alivisatos, A. P. Cation Exchange Reactions in Ionic Nanocrystals. *Science* **2004**, *306*, 1009–1012.
- (15) De Trizio, L.; Manna, L. Forging Colloidal Nanostructures *via* Cation Exchange Reactions. *Chem. Rev.* **2016**, *116*, 10852–10887.

- (16) Gupta, S.; Kershaw, S. V.; Rogach, A. L. 25th Anniversary Article: Ion Exchange in Colloidal Nanocrystals. *Adv. Mater.* **2013**, *25*, 6923–6944.
- (17) Beberwyck, B. J.; Surendranath, Y.; Alivisatos, A. P. Cation Exchange: A Versatile Tool for Nanomaterials Synthesis. *J. Phys. Chem. C* **2013**, *117*, 19759–19770.
- (18) Plante, I. J. L.; Teitelboim, A.; Pinkas, I.; Oron, D.; Mokari, T. Exciton Quenching Due to Copper Diffusion Limits the Photocatalytic Activity of CdS/Cu₂S Nanorod Heterostructures. *J. Phys. Chem. Lett.* **2014**, *5*, 590–596.
- (19) Lesnyak, V.; Brescia, R.; Messina, G. C.; Manna, L. Cu Vacancies Boost Cation Exchange Reactions in Copper Selenide Nanocrystals. *J. Am. Chem. Soc.* **2015**, *137*, 9315–9323.
- (20) Meir, N.; Martín-García, B.; Moreels, I.; Oron, D. Revisiting the Anion Framework Conservation in Cation Exchange Processes. *Chem. Mater.* **2016**, *28*, 7872–7877.
- (21) Kubas, G. J.; Monzyk, B.; Crumbliss, A. L. Tetrakis-(Acetonitrile)Copper(I) Hexafluorophosphate. *Inorg. Synth.* **1979**, *19*, 90–92.
- (22) Zou, Y.; Sun, C.; Gong, W.; Yang, X.; Huang, X.; Yang, T.; Lu, W.; Jiang, J. Morphology-Controlled Synthesis of Hybrid Nanocrystals via a Selenium-Mediated Strategy with Ligand Shielding Effect: The Case of Dual Plasmonic Au–Cu_{2–x}Se. *ACS Nano* **2017**, *11*, 3776–3785.
- (23) Xia, Y.; Nguyen, T. D.; Yang, M.; Lee, B.; Santos, A.; Podsiadlo, P.; Tang, Z.; Glotzer, S. C.; Kotov, N. A. Self-Assembly of Self-Limiting Monodisperse Supraparticles from Polydisperse Nanoparticles. *Nat. Nanotechnol.* **2011**, *6*, 580–587.
- (24) Zhao, Y.; Pan, H.; Lou, Y.; Qiu, X.; Zhu, J. Plasmonic Cu_{2–x}S Nanocrystals: Optical and Structural Properties of Copper-Deficient Copper(I) Sulfides. *J. Am. Chem. Soc.* **2009**, *131*, 4253–4261.
- (25) Jain, P. K.; Manthiram, K.; Engel, J. H.; White, S. L.; Fauchaux, J. A.; Alivisatos, A. P. Doped Nanocrystals as Plasmonic Probes of Redox Chemistry. *Angew. Chem., Int. Ed.* **2013**, *52*, 13671–13675.
- (26) Welscher, K.; Liu, Z.; Sherlock, S. P.; Robinson, J. T.; Chen, Z.; Daranciang, D.; Dai, H. A Route to Brightly Fluorescent Carbon Nanotubes for Near-Infrared Imaging in Mice. *Nat. Nanotechnol.* **2009**, *4*, 773–780.
- (27) Hong, G.; Robinson, J. T.; Zhang, Y.; Diao, S.; Antaris, A. L.; Wang, Q.; Dai, H. *In Vivo* Fluorescence Imaging with Ag₂S Quantum Dots in the Second Near-Infrared Region. *Angew. Chem.* **2012**, *124*, 9956–9959.
- (28) Wang, Y.; Black, K. C. L.; Luehmann, H.; Li, W.; Zhang, Y.; Cai, X.; Wan, D.; Liu, S. Y.; Li, M.; Kim, P.; Li, Z. Y.; Wang, L. V.; Liu, Y.; Xia, Y. Comparison Study of Gold Nanohexapods, Nanorods, and Nanocages for Photothermal Cancer Treatment. *ACS Nano* **2013**, *7*, 2068–2077.
- (29) Petros, R. A.; Desimone, J. M. Strategies in the Design of Nanoparticles for Therapeutic Applications. *Nat. Rev. Drug Discovery* **2010**, *9*, 615–627.
- (30) Zhang, S.; Sun, C.; Zeng, J.; Sun, Q.; Wang, G.; Wang, Y.; Wu, Y.; Dou, S.; Gao, M.; Li, Z. Ambient Aqueous Synthesis of Ultrasmall PEGylated Cu_{2–x}Se Nanoparticles as a Multifunctional Theranostic Agent for Multimodal Imaging Guided Photothermal Therapy of Cancer. *Adv. Mater.* **2016**, *28*, 8927–8936.
- (31) Wang, Y.; Wu, Y.; Liu, Y.; Shen, J.; Lv, L.; Li, L.; Yang, L.; Zeng, J.; Wang, Y.; Zhang, L. W.; Li, Z.; Gao, M.; Chai, Z. BSA-Mediated Synthesis of Bismuth Sulfide Nanotheranostic Agents for Tumor Multimodal Imaging and Thermoradiotherapy. *Adv. Funct. Mater.* **2016**, *26*, 5335–5344.
- (32) Weber, J.; Beard, P. C.; Bohndiek, S. E. Contrast Agents for Molecular Photoacoustic Imaging. *Nat. Methods* **2016**, *13*, 639–650.
- (33) Dou, Y.; Guo, Y.; Li, X.; Li, X.; Wang, S.; Wang, L.; Lv, G.; Zhang, X.; Wang, H.; Gong, X.; Chang, J. Size-Tuning Ionization to Optimize Gold Nanoparticles for Simultaneous Enhanced CT Imaging and Radiotherapy. *ACS Nano* **2016**, *10*, 2536–2548.
- (34) Gao, J.; Chen, K.; Luong, R.; Bouley, D. M.; Mao, H.; Qiao, T.; Gambhir, S. S.; Cheng, Z. A Novel Clinically Translatable Fluorescent Nanoparticle for Targeted Molecular Imaging of Tumors in Living Subjects. *Nano Lett.* **2012**, *12*, 281–286.
- (35) Ji, X.; Song, X.; Li, J.; Bai, Y.; Yang, W.; Peng, X. Size Control of Gold Nanocrystals in Citrate Reduction: The Third Role of Citrate. *J. Am. Chem. Soc.* **2007**, *129*, 13939–13948.
- (36) Nikoobakht, B.; El-Sayed, M. A. Preparation and Growth Mechanism of Gold Nanorods (NRs) Using Seed-Mediated Growth Method. *Chem. Mater.* **2003**, *15*, 1957–1962.
- (37) Lu, L.; Xia, Y. Enzymatic Reaction Modulated Gold Nanorod End-to-End Self-Assembly for Ultrahigh Sensitivity Colorimetric Sensing of Cholinesterase and Organophosphate Pesticides in Human Blood. *Anal. Chem.* **2015**, *87*, 8584–8591.
- (38) Roper, D. K.; Ahn, W.; Hoepfner, M. Microscale Heat Transfer Transduced by Surface Plasmon Resonant Gold Nanoparticles. *J. Phys. Chem. C* **2007**, *111*, 3636–3641.